remote sensing

MDPI

Article

Real Micro-Doppler Parameters Extraction of Spinning Targets Based on Rotating Interference Antenna

Zhihao Wang [1], Yijun Chen [2,3,*], Hang Yuan [1], Ying Luo [1] and Qun Zhang [1]

[1] Information and Navigation College, Air Force Engineering University, Xi'an 710077, China
[2] The National Lab of Radar Signal Processing, Xidian University, Xi'an 710071, China
[3] College of Information Engineering, Engineering University of PAP, Xi'an 710086, China
* Correspondence: chenyijun519@126.com

Abstract: Micro-Doppler is a unique characteristic of targets with micro-motions, which can provide significant information for target classification and recognition. However, the monostatic radar has the shortcoming of only obtaining the radial micro-motion characteristics. Although the vortex-electromagnetic-wave-based radar has the potential to obtain real micro-motion parameters, it has a high dependence on the mode number and purity of the orbital angular momentum, which greatly restricts its application in the micro-motion parameter extraction. To overcome the above problems, a new radar configuration based on the rotating interference antenna is proposed in this paper. Through the interference processing of the micro-Doppler curves of the rotating and fixed antenna, the curves containing the real micro-motion information of the target can be obtained. Then the real micro-motion characteristics of the spinning target can be reconstructed by the orthogonal matching pursuit algorithm. The effectiveness and robustness of the proposed method are validated by simulations.

Keywords: rotating interference antenna; spinning targets; micro-Doppler parameters extraction; OMP algorithm

Citation: Wang, Z.; Chen, Y.; Yuan, H.; Luo, Y.; Zhang, Q. Real Micro-Doppler Parameters Extraction of Spinning Targets Based on Rotating Interference Antenna. *Remote Sens.* **2022**, *14*, 5300. https://doi.org/10.3390/rs14215300

Academic Editor: Stefano Perna

Received: 23 August 2022
Accepted: 20 October 2022
Published: 23 October 2022

1. Introduction

The micro-motion of the radar target itself or its structural components will introduce a frequency modulation to the radar echo signal. This frequency modulation is called micro-Doppler [1,2]. The micro-Doppler effect is considered a unique characteristic of the targets with micro-motions, which can provide important information for target classification and recognition. The phenomenon has been widely researched in the classification and recognition of ballistic and rotor targets [3–9]. In addition, the micro-Doppler effect is also widely applied to the fields of human gait and gesture recognition [10–13].

The micro-Doppler effect has been studied extensively in monostatic radar. In [1], the concept of the micro-Doppler effect was first introduced into the radar field, and the mathematical model of targets with micro-motions in monostatic radar was established. In [14], the standard Hough transform (HT) was used to detect the straight line in the time-frequency (TF) domain, namely the Doppler curves of rigid scatterers. Moreover, the extended HT (EHT) with four parameters in the Hough space was put forward for sinusoid detection and estimation and the subsequent elimination of rotating components from the spectrogram. Unfortunately, under the condition of monostatic radar, the parameters of the micro-Doppler curve are determined by the projection value of the motion vector in the direction of the radar line of sight (LOS), so the monostatic radar can only extract the geometric and micro-motion parameters in the radar LOS. The radar perspective will change with the movement of the target. Therefore, the micro-Doppler parameters of the same target under different radar perspectives will show significant differences, which will affect the accuracy of target recognition. Taking the spinning target as an example, although the rotational frequency can be effectively obtained in the monostatic radar, the

real rotational radius and tilt angle are coupled together and cannot be effectively separated. Therefore, to overcome the azimuth sensitivity of the micro-Doppler characteristic, it is necessary to obtain the real micro-motion information that does not change with the radar LOS.

The vortex electromagnetic waves have been utilized in radar target detection and recognition in recent years [15–17]. Vortex electromagnetic waves carry the orbital angular momentum (OAM). Different from traditional plane waves, the OAM has the helical phase wavefront distribution. The change of target azimuth angle will generate the angular Doppler, which can also be called the rotational Doppler. The angular Doppler can provide extra information for radar target detection and recognition. It provides a new solution for multi-dimensional micro-motion feature extraction [18–22]. Ref. [20] deduced the angular Doppler shift expression of the spinning target in an arbitrary position and gave the parameterized expression of the rotation radius or tilt angle in two special scenarios; namely, the tilt angle is zero, and the rotation center is on the Y-axis. It proves that the vortex-electromagnetic-wave-based radar has a great prospect in micro-motion feature extraction. In [21], the detection of the angular Doppler in arbitrary positions is researched. After extracting the angular Doppler curve from the total Doppler curve in the time-frequency domain, the real rotational radius and tilt angle can be obtained by applying the EHT to the angular Doppler. However, this method only considers the case of one scatterer; the case of multiple scatterers needs to be further studied. Moreover, when the angular Doppler is less than the resolution of TF analysis, the image processing method is not applicable. At present, the configuration of the vortex-electromagnetic-wave-based radar is mainly the uniform circular array (UCA). It is easy for UCA to change the phase and quickly regulate the mode number of OAM. As is known to all, the angular Doppler is positively correlated with the mode number of OAM. To ensure the accuracy of micro-motion feature extraction, the angular Doppler should be greater than the resolution of the TF analysis. Therefore, the mode number of OAM is required to be high. However, according to [23,24], the larger the mode number is, the more antennas of the array are required. With the use of the UCA-based OAM generation method, it is difficult to obtain the pure multi-mode vortex electromagnetic waves, which restricts the development of micro-motion parameters extraction by using vortex-electromagnetic-wave-based radar to a certain extent.

To overcome the above problems, a new method for extracting the real micro-motion parameters of spinning targets based on rotating interference antennas is proposed in this paper. Firstly, a new radar configuration based on a rotating interference antenna is proposed. There is an antenna rotating around the coordinate center at a constant speed, and another antenna is fixed at the coordinate center. Each of the two antennas transmits single-frequency continuous wave signals with the same carrier frequency, and then the curve containing the real micro-motion information can be obtained by the two micro-Doppler curves' subtraction. Finally, the OMP algorithm is utilized to reconstruct the parameters of the desired curve, which can invert the real micro-motion parameters of the spinning target.

The rest of this paper is organized as follows. In Section 2, the radar observation model based on a rotating interference antenna is established, and the equations of micro-Doppler frequency shift are derived and validated. In Section 3, a real micro-motion parameters extraction method based on the OMP algorithm is proposed. In Section 4, simulations are conducted to verify the effectiveness and robustness of the proposed method. Conclusions are drawn in Section 5.

2. Radar Observation Model and Micro-Doppler Effect

As shown in Figure 1, $OXYZ$ is the radar Cartesian coordinate system, and the origin O' of the reference coordinate system $O'X'Y'Z'$, which is parallel to the radar coordinate system, is located at $(x_0, y_0, z_0)^{\mathrm{T}}$ in $OXYZ$, where the superscript "T" denotes the transposition of the vector. The range from O to O' can be expressed as $R_0 = \sqrt{x^2{}_0 + y^2{}_0 + z^2{}_0}$. The target-local coordinate system $O'xyz$ shares the same origin O' with the reference coordinate

system $O'X'Y'Z'$. In $OXYZ$, the antenna Q rotates in a counterclockwise direction around the origin O, with the rotation frequency of f_a and radius of a. Therefore, the Cartesian coordinate of Q at time t in $OXYZ$ can be expressed as $\boldsymbol{OQ} = (a \cdot \cos(2\pi f_a t),\ a \cdot \sin(2\pi f_a t), 0)^{\mathrm{T}}$. The scatterer P rotates on the $xO'y$ plane around the z-axis with a rotational frequency of f_c and radius of r_a. Therefore, the Cartesian coordinate of P at time t in $O'xyz$ can be expressed as $\boldsymbol{O'P} = (r_a \cos(2\pi f_c t + \eta),\ r_a \sin(2\pi f_c t + \eta), 0)^{\mathrm{T}}$, where η represents the initial azimuth of P in $O'xyz$.

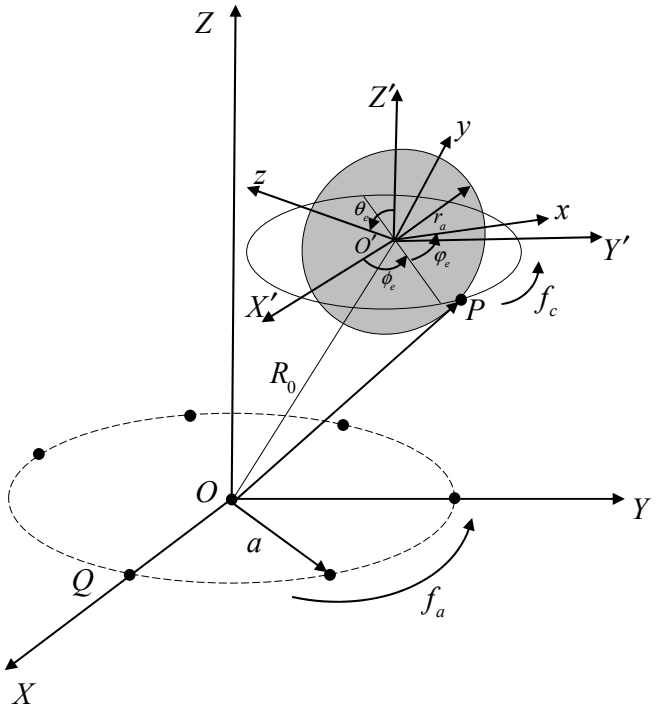

Figure 1. The geometric relationship between the radar and spinning target.

Assume the Euler angle between $O'X'Y'Z'$ and $O'xyz$ is φ_e, θ_e, and ψ_e, i.e., the reference coordinate system can be transformed to the target-local coordinate system by rotating about the Z'-axis for φ_e, the X'-axis for θ_e, and the Z'-axis again for ψ_e. The initial Euler matrix $\boldsymbol{R}_{init}$ can be expressed as

$$\begin{aligned}\boldsymbol{R}_{init} &= \begin{bmatrix}\cos\psi_e & -\sin\psi_e & 0\\ \sin\psi_e & \cos\psi_e & 0\\ 0 & 0 & 1\end{bmatrix}\begin{bmatrix}1 & 0 & 0\\ 0 & \cos\theta_e & -\sin\theta_e\\ 0 & \sin\theta_e & \cos\theta_e\end{bmatrix}\begin{bmatrix}\cos\varphi_e & -\sin\varphi_e & 0\\ \sin\varphi_e & \cos\varphi_e & 0\\ 0 & 0 & 1\end{bmatrix}\\ &= \begin{bmatrix}a_{11} & a_{12} & a_{13}\\ a_{21} & a_{22} & a_{23}\\ a_{31} & a_{32} & a_{33}\end{bmatrix}\end{aligned} \tag{1}$$

$$\begin{cases} a_{11} = \cos\psi_e\cos\varphi_e - \sin\psi_e\cos\theta_e\sin\varphi_e\\ a_{12} = -\cos\psi_e\sin\varphi_e - \sin\psi_e\cos\theta_e\cos\varphi_e\\ a_{13} = \sin\psi_e\sin\theta_e\\ a_{21} = \sin\psi_e\cos\varphi_e + \cos\psi_e\cos\theta_e\sin\varphi_e\\ a_{22} = -\sin\psi_e\sin\varphi_e + \cos\psi_e\cos\theta_e\cos\varphi_e\\ a_{23} = -\cos\psi_e\sin\theta_e\\ a_{31} = \sin\theta_e\sin\varphi_e\\ a_{32} = \sin\theta_e\cos\varphi_e\\ a_{33} = \cos\theta_e \end{cases} \tag{2}$$

The position of P in $OXYZ$ can be expressed as

$$\begin{aligned} \boldsymbol{OP} &= \boldsymbol{OO'} + \boldsymbol{R}_{init} \times \boldsymbol{O'P} \\ &= \begin{pmatrix} a_{11} r_a \cos(2\pi f_c t + \eta) + a_{12} r_a \sin(2\pi f_c t + \eta) + x_0 \\ a_{21} r_a \cos(2\pi f_c t + \eta) + a_{22} r_a \sin(2\pi f_c t + \eta) + y_0 \\ a_{31} r_a \cos(2\pi f_c t + \eta) + a_{32} r_a \sin(2\pi f_c t + \eta) + z_0 \end{pmatrix} \end{aligned} \tag{3}$$

Therefore, the range $r_{p1}(t)$ between Q and P is

$$\begin{aligned} & r_{p1}(t) = \|\boldsymbol{OQ} - \boldsymbol{OP}\| \\ & = \sqrt{\begin{array}{l} a^2 + {r_a}^2 + {R_0}^2 + 2 r_a A_1 \cos(2\pi f_c t - \varphi_1) - 2 a r_0 \cos(2\pi f_a t - \varphi_0) \\ -a r_a((1 + \cos\theta_e)\cos(2\pi(f_c - f_a)t + \psi_1) + (1 - \cos\theta_e)\cos(2\pi(f_c + f_a)t - \psi_2)) \end{array}} \end{aligned} \tag{4}$$

$$\begin{cases} A_1 = \sqrt{(x_0 a_{11} + y_0 a_{12} + z_0 a_{13})^2 + (x_0 a_{21} + y_0 a_{22} + z_0 a_{23})^2} \\ \varphi_1 = \arctan\left(\frac{x_0 a_{21} + y_0 a_{22} + z_0 a_{23}}{x_0 a_{11} + y_0 a_{12} + z_0 a_{13}}\right) + \eta \\ r_0 = \sqrt{{x_0}^2 + {y_0}^2} \\ \varphi_0 = \arctan\left(\frac{y_0}{x_0}\right) \\ \psi_1 = \psi_e + \varphi_e + \eta \\ \psi_2 = \psi_e - \varphi_e - \eta \end{cases} \tag{5}$$

Through the Fresnel approximation processing of the above range equation, the approximate range can be obtained as

$$\begin{aligned} r_{p1}(t) \quad & \approx R_0 + \tfrac{a^2 + {r_a}^2}{2R_0} + \tfrac{r_a A_1}{R_0}\cos(2\pi f_c t - \varphi_1) - \tfrac{a r_0}{R_0}\cos(2\pi f_a t - \varphi_0) \\ & - \left(\tfrac{a r_a}{2R_0}(1 + \cos\theta_e)\cos(2\pi(f_c - f_a)t + \psi_1) + \tfrac{a r_a}{2R_0}(1 - \cos\theta_e)\cos(2\pi(f_c + f_a)t - \psi_2)\right) \end{aligned} \tag{6}$$

Similarly, the range $r_{p1}(t)$ between O and P can be approximated as

$$\begin{aligned} r_{p0}(t) \quad & = \sqrt{{r_a}^2 + {R_0}^2 + 2 r_a A_1 \cos(2\pi f_c t - \varphi_1)} \\ & \approx R_0 + \tfrac{{r_a}^2}{2R_0} + \tfrac{r_a A_1}{R_0}\cos(2\pi f_c t - \varphi_1) \end{aligned} \tag{7}$$

Both the rotating antenna and the fixed antenna radiate single-frequency continuous wave signals with the same carrier frequency f_0. The wavelengths of the signals are both $\lambda = \frac{f_0}{c}$. Therefore, the echo expressions of the rotating antenna and the fixed antenna can be respectively expressed as

$$s_{echo1}(t) = \exp\left(\mathrm{j}\frac{4\pi}{\lambda} r_{p1}(t)\right) \tag{8}$$

$$s_{echo0}(t) = \exp\left(\mathrm{j}\frac{4\pi}{\lambda} r_{p0}(t)\right) \tag{9}$$

When there is only one scatterer, the conjugate of $s_{echo0}(t)$ can be multiplied by $s_{echo1}(t)$ to achieve the elimination of signal component with frequency f_c, namely

$$\begin{aligned} & s_{inter}(t) = s_{echo1}(t) \cdot {s^*}_{echo0}(t) \\ & = \exp\left(\mathrm{j}\tfrac{4\pi}{\lambda}\left(\tfrac{a^2}{2R_0} - \tfrac{a r_0}{R_0}\cos(2\pi f_a t - \varphi_0)\right)\right) \cdot \\ & \exp\left(-\mathrm{j}\tfrac{4\pi}{\lambda}\left(\tfrac{a r_a}{2R_0}(1 + \cos\theta_e)\cos(2\pi(f_c - f_a)t + \psi_1) + \tfrac{a r_a}{2R_0}(1 - \cos\theta_e)\cos(2\pi(f_c + f_a)t - \psi_2)\right)\right) \end{aligned} \tag{10}$$

where "*" represents the conjugate multiplication operation. Since the rotating frequency of Q is known, the frequency component with frequency f_a can be filtered by passing $s_{inter}(t)$ through the filter, and the desired echo signal can be obtained.

$$s_c(t) = \exp\left(\mathrm{j}\frac{4\pi}{\lambda}\left(\frac{a^2}{2R_0} - \left(\frac{ar_a}{2R_0}(1+\cos\theta_e)\cos(2\pi(f_c - f_a)t + \psi_1) + \frac{ar_a}{2R_0}(1-\cos\theta_e)\cos(2\pi(f_c + f_a)t - \psi_2)\right)\right)\right) \quad (11)$$

Assuming that there are L spinning scatterers, the interference of the echo phase will produce cross terms.

$$\begin{aligned} s_{inter}(t) &= s_{echo1}(t) \cdot s^*_{echo0}(t) = \sum_{i=1}^{L} \exp\left(\mathrm{j}\tfrac{4\pi}{\lambda} r_{p1i}(t)\right) \cdot \sum_{i=1}^{L} \exp\left(\mathrm{j}\tfrac{4\pi}{\lambda} r_{p0i}(t)\right) \\ &= \sum_{i=1}^{L}\left(\exp\left(\mathrm{j}\tfrac{4\pi}{\lambda} r_{p1i}(t)\right) \cdot \exp\left(\mathrm{j}\tfrac{4\pi}{\lambda} r_{p0i}(t)\right)\right) + \sum_{i,j=1, j\neq i}^{L}\left(\exp\left(\mathrm{j}\tfrac{4\pi}{\lambda} r_{p1i}(t)\right) \cdot \exp\left(\mathrm{j}\tfrac{4\pi}{\lambda} r_{p0j}(t)\right)\right) \end{aligned} \quad (12)$$

where $\sum_{i=1}^{L}\left(\exp\left(\mathrm{j}\frac{4\pi}{\lambda} r_{p1i}(t)\right) \cdot \exp\left(-\mathrm{j}\frac{4\pi}{\lambda} r_{p0i}(t)\right)\right)$ represents the result after echo phase interference of the same target. There are L terms in total, which are called the "uncross terms" in this paper. $\sum_{i,j=1, j\neq i}^{L}\left(\exp\left(\mathrm{j}\frac{4\pi}{\lambda} r_{p1i}(t)\right) \cdot \exp\left(-\mathrm{j}\frac{4\pi}{\lambda} r_{p0j}(t)\right)\right)$ represents the result after echo phase interference of the different targets, and there are L·(L-1) terms in total, which are called the "cross terms" in this paper. The cross terms have a great influence on the micro-Doppler signal and cannot be ignored. Therefore, the micro-Doppler curves' subtraction in the time-frequency domain is chosen to extract the real micro-Doppler parameters of multiple spinning scatterers in this paper. The micro-Doppler expressions $f_{d1}(t)$ and $f_{d0}(t)$ can be obtained by taking the derivative of the echo phases of the rotating and fixed antenna, respectively.

$$f_{d1}(t) = \frac{4\pi}{\lambda}\left(-\frac{r_a A_1 f_c}{R_0}\sin(2\pi f_c t - \varphi_1) + \frac{ar_0 f_a}{R_0}\sin(2\pi f_a t - \varphi_0) + (B_1\sin(2\pi(f_c - f_a)t + \psi_1) + B_2\sin(2\pi(f_c + f_a)t - \psi_2))\right) \quad (13)$$

$$f_{d0}(t) = \frac{4\pi}{\lambda}\left(-\frac{r_a A_1 f_c}{R_0}\sin(2\pi f_c t - \varphi_1)\right) \quad (14)$$

where $B_1 = \frac{ar_a}{2R_0}(1+\cos\theta_e)(f_c - f_a)$ and $B_2 = \frac{ar_a}{2R_0}(1-\cos\theta_e)(f_c + f_a)$. After subtracting $f_{d0}(t)$ from $f_{d1}(t)$, the desired micro-Doppler expression can be obtained by passing the filter with blocking frequency f_a.

$$f_d(t) = \frac{4\pi}{\lambda}(B_1\sin(2\pi(f_c - f_a)t + \psi_1) + B_2\sin(2\pi(f_c + f_a)t - \psi_2)) \quad (15)$$

It can be seen from Equation (15) that the desired micro-Doppler curve is superimposed by two sinusoidal signals with different amplitudes, frequencies, and initial phases.

3. Extraction Method of Real Micro-Motion Parameters

3.1. Curves Separation and Smoothing

Assuming that there are multiple scatterers. The conjugate of $s_{echo0}(t)$ is multiplied with $s_{echo1}(t)$ in the time domain, and the cross term will cause a great interference to the subsequent micro-motion features extraction. The short-time Fourier transform (STFT) is applied to the echo signals after conjugate multiplication, and the results are shown in Figure 2. It can be seen that the Doppler frequency shift of the cross-term is very obvious. Therefore, in the case of multiple scatterers, it is difficult to process the Doppler shift in the time domain. Therefore, the Doppler shift should be processed in the time-frequency domain. The micro-Doppler curves of the rotating and fixed antenna can be obtained after the STFT, and the smoothness of the curves is utilized to separate the micro-Doppler curves of different scatterers, which can avoid the interference of cross terms.

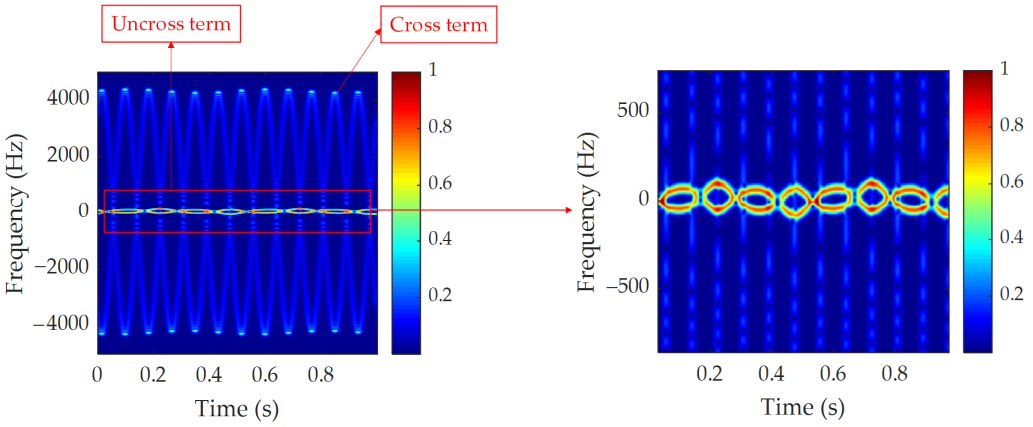

Figure 2. The STFT image of the echo signals after conjugate multiplication when there are multiple scatterers.

In order to improve the accuracy of the TF analysis, the skeleton extraction algorithm is used for the micro-Doppler curves in the TF domain. Firstly, the micro-Doppler curves are smoothed by the Gaussian mask to make the curve reach the condition of ideal smoothness. Then, an appropriate threshold is set to transform it into a binary image, and the skeletons of the micro-Doppler curves are extracted on this basis.

After extracting the skeletons, the micro-Doppler curves can be separated. In this paper, the smoothness of the curves is used to realize the separation of micro-Doppler curves. Since the curve separation algorithm is not the main innovation point of this paper, it is not necessary to be described here, and the specific algorithm process can refer to [25].

The separated micro-Doppler curves are subtracted to eliminate the signal components with frequency f_c. The "burr" will appear on the subtracted curve. It is necessary to smooth the subtracted curves. In the process of smoothing, the local regression using weighted linear least squares and a 2nd-degree polynomial model is adopted, and the corresponding method in the smooth function of MATLAB is "Loess".

3.2. Real Micro-Motion Parameters Estimation

In this paper, the OMP algorithm is used to decompose and reconstruct the micro-Doppler signal. Before the OMP algorithm, it is essential to perform autocorrelation processing on the micro-Doppler curve of the fixed antenna to obtain the estimated value of the rotational frequency so as to reduce the number of parameters to be reconstructed in the OMP algorithm and save computing resources.

According to the principle of the OMP algorithm, the atomic set in the dictionary should be constructed according to the intrinsic characteristics of the signal to be decomposed [26]. According to Equation (15), the atom set can be constructed by setting different values of $(C_1, C_2, \psi_1, \psi_2)$, and the kth atom in the atom set can be expressed as

$$\boldsymbol{f_d}^{(k)} = {C_1}^{(k)} \sin\left(2\pi(f_c - f_a)t + {\psi_1}^{(k)}\right) + {C_2}^{(k)} \sin\left(2\pi(f_c + f_a)t - {\psi_2}^{(k)}\right) \tag{16}$$

$$C_1 = \frac{2\pi a r_a}{\lambda R_0}(1 + \cos\theta_e)(f_c - f_a) \tag{17}$$

$$C_2 = \frac{2\pi a r_a}{\lambda R_0}(1 - \cos\theta_e)(f_c + f_a) \tag{18}$$

The energy of each atom in the atom set is normalized (i.e., $\boldsymbol{f}^{(k)} = \frac{{f_d}^{(k)}}{\|{f_d}^{(k)}\|_{\mathrm{F}}}$). $\|{\boldsymbol{f}_d}^{(k)}\|_{\mathrm{F}}$ denotes the Fibonacci norm of ${\boldsymbol{f}_d}^{(k)}$. Assuming that ${C_1}^{(k)} \in [C_{1\min}, C_{1\max}]$, ${C_2}^{(k)} \in [C_{2\min}, C_{2\max}]$, ${\psi_1}^{(k)} \in [\psi_{1\min}, \psi_{1\max}]$ and ${\psi_2}^{(k)} \in [\psi_{2\min}, \psi_{2\max}]$. The search steps are ΔC_1, ΔC_2, $\Delta\psi_1$, and $\Delta\psi_2$, respectively. Therefore, the number F_b of atoms in the atom set can be written as

$$F_b = \left(\left\lfloor \frac{C_{1\max} - C_{1\min}}{\Delta C_1} \right\rfloor + 1\right) \cdot \left(\left\lfloor \frac{C_{2\max} - C_{2\min}}{\Delta C_2} \right\rfloor + 1\right) \cdot \left(\left\lfloor \frac{\psi_{1\max} - \psi_{1\min}}{\Delta \psi_1} \right\rfloor + 1\right) \cdot \left(\left\lfloor \frac{\psi_{2\max} - \psi_{2\min}}{\Delta \psi_2} \right\rfloor + 1\right) \quad (19)$$

where $\lfloor \cdot \rfloor$ denotes the symbol of rounding down.

After the values of $(\hat{C}_1, \hat{C}_2, \hat{\psi}_1, \hat{\psi}_2)$ are obtained, the value of the rotational radius can be estimated by combining (17) and (18).

$$\hat{\theta}_e = \operatorname{acos}\left(\frac{(f_c + f_a)C_1 - (f_c - f_a)C_2}{(f_c + f_a)C_1 + (f_c - f_a)C_2}\right) \quad (20)$$

The estimated value of the tilt angle can be obtained by substituting (20) into (17) or (18).

$$\hat{r}_a = \frac{\lambda R_0 C_1}{2\pi a(1 + \cos\hat{\theta}_e)(f_c - f_a)} \text{ or } \hat{r}_a = \frac{\lambda R_0 C_2}{2\pi a(1 - \cos\hat{\theta}_e)(f_c + f_a)} \quad (21)$$

The flow chart of the proposed method is shown in Figure 3.

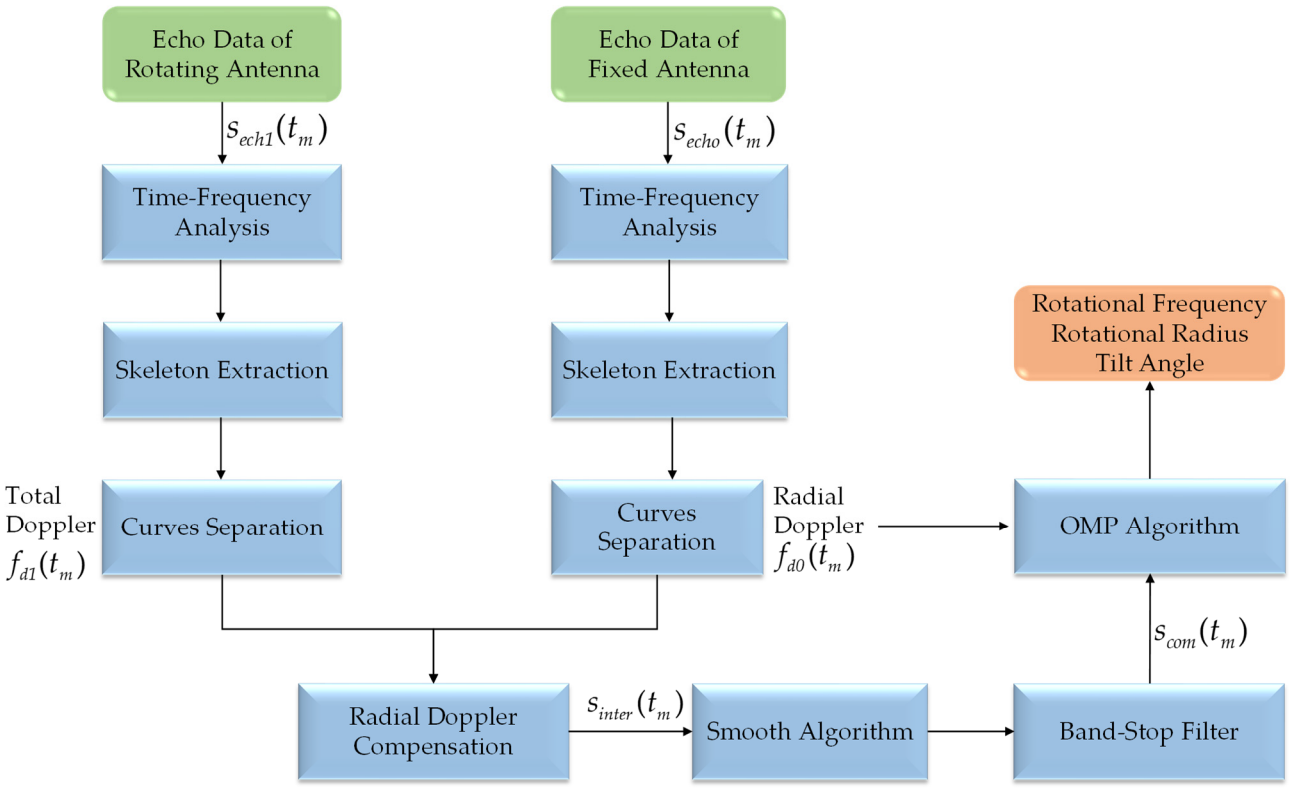

Figure 3. The flow chart of the proposed method.

4. Simulations and Discussions

In order to verify the effectiveness and robustness of the proposed method, two scatterers P_1 and P_2 are set in this section. The parameters of radar and spinning scatterers are set as shown in Table 1. The rotating and the fixed antenna transmit single-frequency signals of the same carrier frequency. Assume that the receiving and transmitting signals of the two antennas are isolated from each other and do not affect each other. The pulse repetition frequencies of the two antennas are both 6000 Hz. In order to be more suited to the practical application, the carrier frequency is set as 35 GHz (one of the atmospheric transmission bands). The initial positions of P_1 and P_2 in $O'xyz$ are (0.5, 0, 0) m and (0, 0.5, 0) m, respectively.

Table 1. Parameters of radar and spinning target.

	Parameter	Symbol	Value
Radar	Carrier frequency	f_0	35 GHz
	Pulse repetition frequency	PRF	6000 Hz
	Rotational radius	a	0.5 m
	Rotating frequency	f_a	2 Hz
	Observation time	t	1 s
Target	Coordinates of the centroid	$(x_0,\ y_0,\ z_0)$	$(0.1,\ 0.2,\ 20)$ m
	Rotational radius	r_a	0.5 m
	Rotational frequency	f_c	6 Hz
	Initial Euler angle	$(\varphi_e,\ \theta_e,\ \psi_e)$	$\left(\frac{2\pi}{9},\ \frac{\pi}{6},\ \frac{\pi}{9}\right)$ rad

4.1. Effectiveness Analysis

Firstly, the effectiveness of the proposed method is investigated. The echo micro-Doppler curves of the fixed antenna (namely the sinusoidal micro-Doppler curve of the traditional monostatic radar) are shown in Figure 4a. The results after the Gaussian mask of 25×25, binarization, and skeleton extraction are shown in Figure 4b, 4c and 4d, respectively. After the skeleton extraction, the curve smoothness is utilized to separate the micro-Doppler curves of the two scatterers, and the results are shown in Figure 4e. The estimated value of rotational frequency can be obtained by applying the autocorrelation processing to the micro-Doppler signal of the fixed antenna. The variation process of the normalized amplitude after autocorrelation processing with time is shown in Figure 4f. The time corresponding to the first peak is the rotational interval, namely 0.1667s. Therefore, the rotational frequency can be estimated at 6 Hz. The rotational radius projected on the radar line of sight direction r_{aLOS} can be expressed as $r_{aLOS} = \frac{\lambda |f_{d0}(t_m)|_{\max}}{4\pi \hat{f}_c} = 0.2438$ m.

The echo micro-Doppler curves of the rotating antenna are shown in Figure 5a. The curves after the Gaussian mask, binarization, and skeleton extraction are shown in Figure 5b, 5c and 5d, respectively. After the skeleton extraction, the smoothness of the curve is used to separate the micro-Doppler curves of the two scatterers, and the results are shown in Figure 5e.

By subtracting the curves in Figure 4e from Figure 5e, the signal component with frequency f_c can be eliminated. The results after curves subtraction are shown in Figure 6a. It can be seen that the "burrs" appear in the subtracted curves. The "Loess" method in the "smooth" function of MATLAB is used to smooth the curves in Figure 6a to eliminate the "burr" phenomenon. The results after smoothing are shown in Figure 6b. In order to reduce the number of parameters to be reconstructed in the OMP algorithm and save computing resources, the filter is used to eliminate the signal component with frequency f_a. The final micro-Doppler curves after passing through the filter are shown in Figure 6c. The corresponding theoretical curves drawn by Equation (15) can be shown in Figure 6d. After curve subtracting, curve smoothing and signal filtering, the final curves are very consistent with the theoretical curves.

Scatterer P_1 is an example that explains the filtering process from Figure 6b to Figure 6c. Fourier transform is applied to the curve after interference processing in the time-frequency domain, and the result is shown in Figure 7a. This signal consists of components with frequencies of 2 Hz, 4 Hz, and 8 Hz, respectively. The rotational frequency of the antenna is 2 Hz, and the high-pass filter is utilized to filter this component. In this paper, the "Highpass" function in Matlab is used for high-pass filtering. The cutoff frequency is 2.5 Hz. The filtered curve is shown in Figure 7b. The curve after passing the high pass filter is basically consistent with the theoretical curve. The corresponding spectrum is shown in Figure 7c. It can be found that the component with a frequency of 2 Hz is filtered out, and the amplitude and phase of other components are well preserved.

Parameters are initialized as follows: $C_{1\min} = 60$, $C_{1\max} = 75$, $\Delta C_1 = 0.2$, $C_{2\min} = 5$, $C_{2\max} = 15$, $\Delta C_2 = 0.2$, $\psi_{1\min} = 0$, $\psi_{1\max} = 2\pi$, $\Delta\psi_1 = 0.025\pi$, $\psi_{2\min} = 0$, $\psi_{2\max} = 2\pi$, and

$\Delta\psi_2 = 0.025\pi$. The energy threshold is set as $\delta = 0.1$. The final micro-Doppler curves of scatterers P_1 and P_2 are decomposed and reconstructed by the OMP algorithm, respectively. After one iteration, the estimated values of $(\hat{C}_1, \hat{C}_2, \hat{\psi}_1, \hat{\psi}_2)$ are shown in Table 2, and the proportions of residual energy are only 0.007% and 0.0014%, respectively, which are both lower than the energy threshold. Therefore, it can be considered that the parameters of the micro-Doppler curves are completely reconstructed after one iteration.

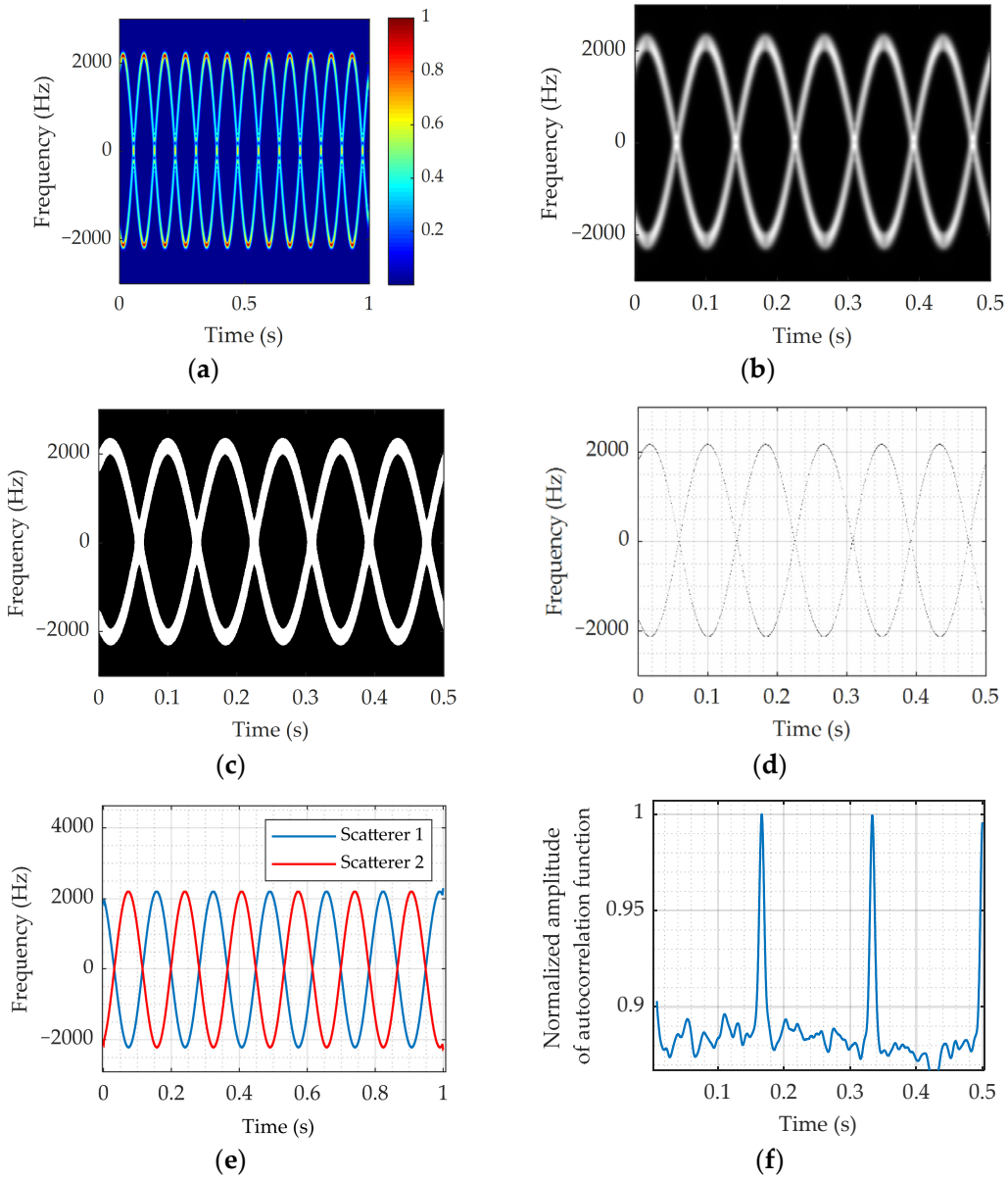

Figure 4. The micro-Doppler effect of the fixed antenna and autocorrelation results. The echo micro-Doppler curves (**a**); The Gaussian mask results (**b**); The binarization results (**c**); The skeleton extraction results (**d**); The micro-Doppler curve separation results (**e**); The variation process of the normalized amplitude with time after autocorrelation processing (**f**).

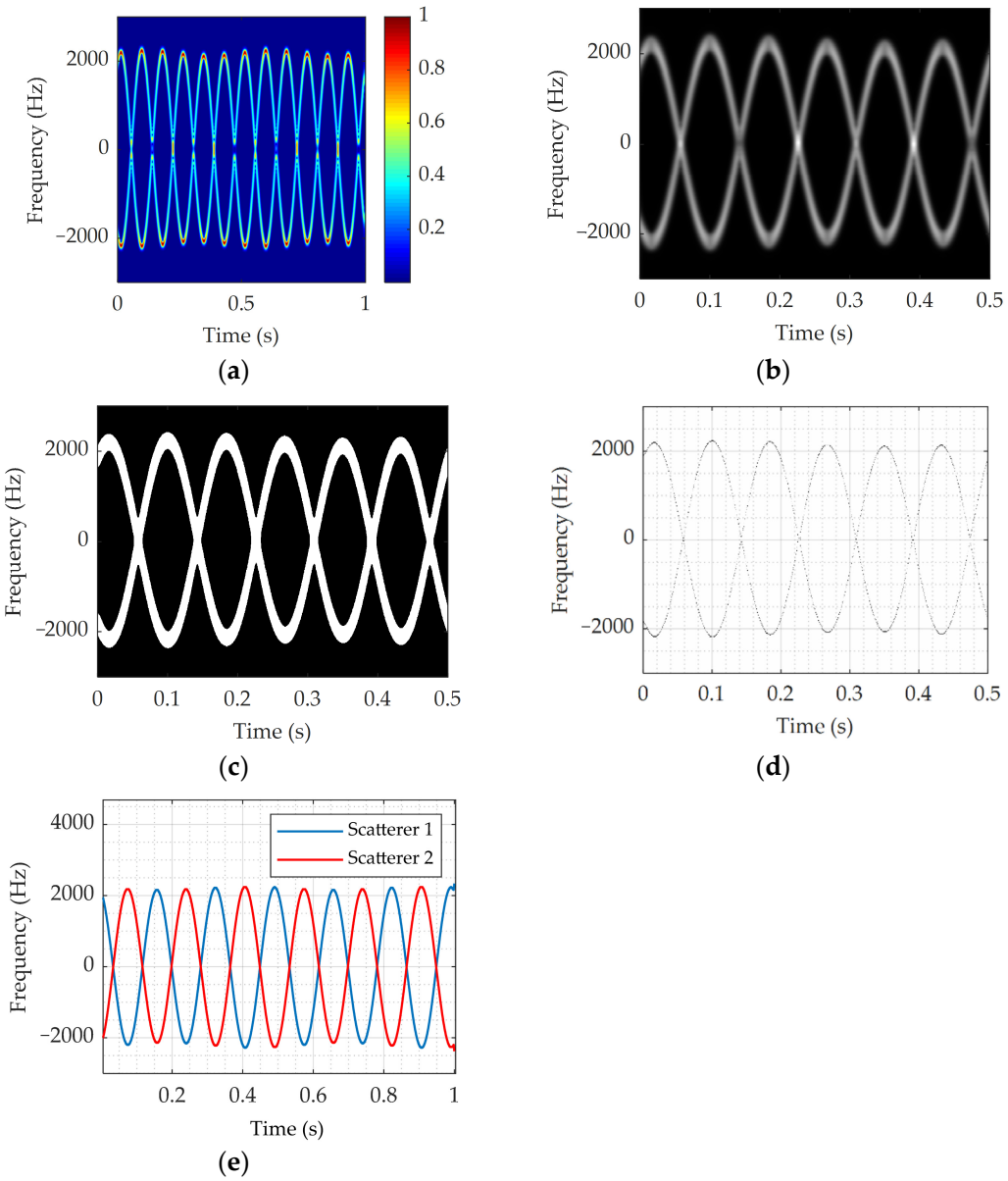

Figure 5. The micro-Doppler effect of the rotating antenna. The echo micro-Doppler curves (**a**); The Gaussian mask results (**b**); The binarization results (**c**); The skeleton extraction results (**d**); The micro-Doppler curve separation results (**e**).

Table 2. The decomposition results of the OMP algorithm.

Parameter	Scatterer 1		Scatterer 2	
	True Value	Estimated Value	True Value	Estimated Value
$\hat{C}_1$	68.4 Hz	70.4 Hz	68.4 Hz	64.4 Hz
$\hat{C}_2$	9.8 Hz	9.8 Hz	9.8 Hz	9.2 Hz
$\hat{\psi}_1$	$\frac{\pi}{3}$ rad	0.35π rad	$\frac{4\pi}{3}$ rad	1.325π rad
$\hat{\psi}_2$	$\frac{\pi}{9}$ rad	0.1π rad	$-\frac{8\pi}{9}$ rad	1.125π rad

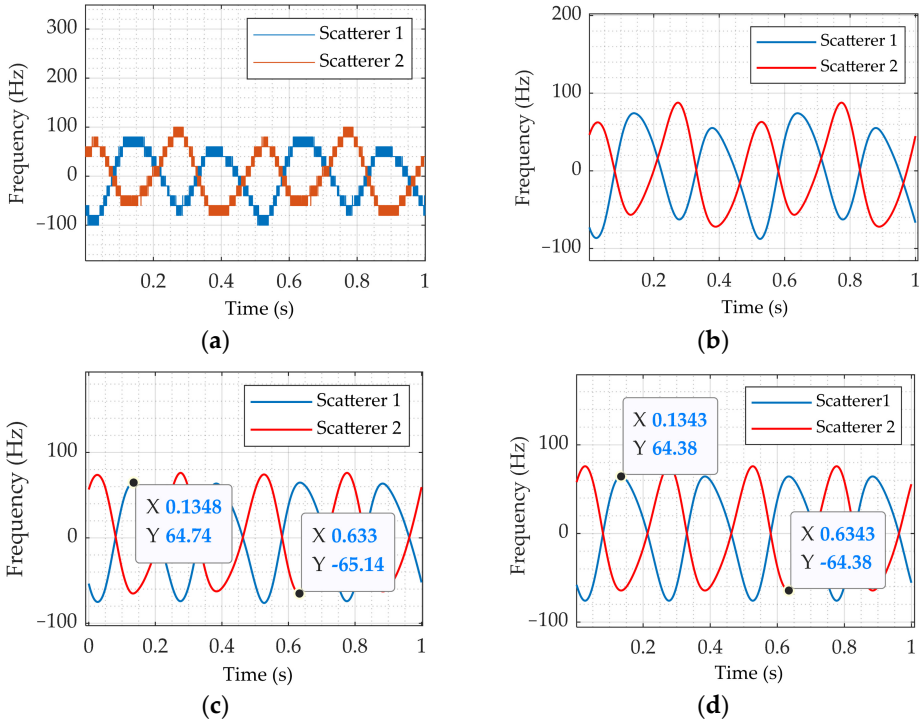

Figure 6. The final micro-Doppler curves of the proposed method. The results after the curves subtraction (**a**); The results after smoothing (**b**); The final micro-Doppler curves (**c**); The theoretical final micro-Doppler curves (**d**).

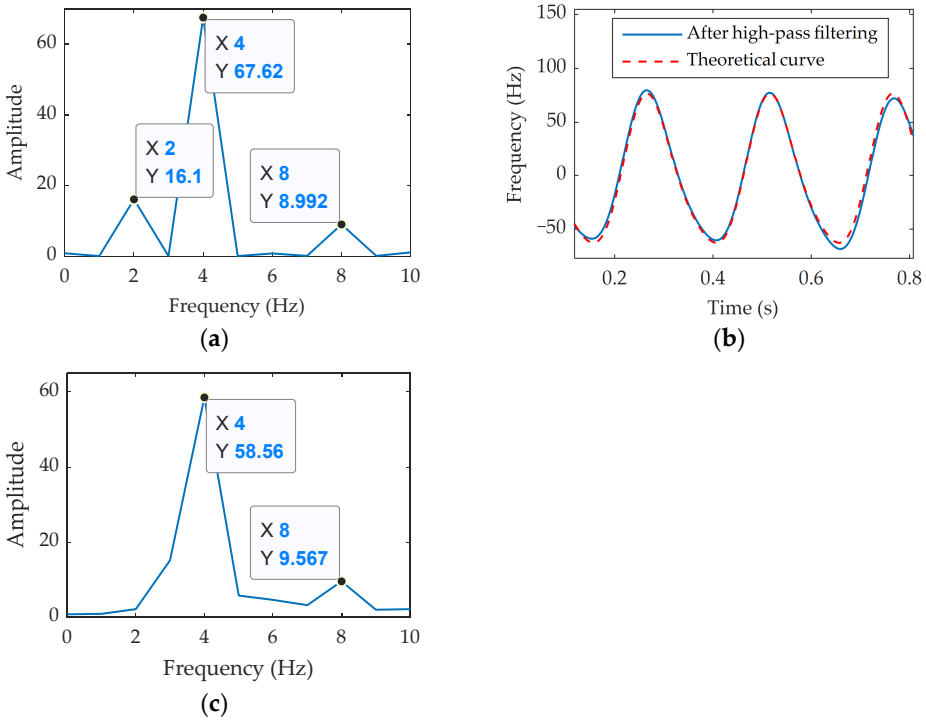

Figure 7. The filtering processing. The spectrum of the curve after interference processing in time-frequency domain (**a**); The filtered curve (**b**); The spectrum of filtered curve (**c**).

The normalized estimation error ρ is introduced to evaluate the estimation performance of the proposed method. The normalized estimation error can be described as

$$\rho = \frac{|X - \hat{X}|}{X} \tag{22}$$

where X represents the true value and $\hat{X}$ represents the estimated value.

According to Equations (20) and (21), the real rotational radius and tilt angle can be estimated. The estimated values of the real rotational radius obtained from P_1 and P_2 are 0.5136 m and 0.4707 m, respectively. The normalized estimation errors are 2.7296% and 5.8653%, respectively, and the average normalized estimation error of the rotational radius is only 4.2975%. The estimated values of the tilt angle of P_1 and P_2 are 0.5159 rad and 0.5223 rad, respectively. The normalized estimation errors are 1.4706% and 0.2483%, respectively, and the average estimation error of the tilt angle is only 0.8595%. The estimated values of $\hat{\psi}_1$ and $\hat{\psi}_2$ from scatterer P_1 and $\hat{\psi}_1$ from scatterer P_2 are consistent with the true values, while the estimated value of $\hat{\psi}_2$ from scatterer P_2 has obvious errors. The reason is that $\hat{\psi}_1$ and $\hat{\psi}_2$ are searched in the interval $[0, 2\pi]$. $\hat{\psi}_1$ and $\hat{\psi}_2$ of P_2 and $\hat{\psi}_1$ of P_2 are all within the interval $[0, 2\pi]$, so the estimated values are consistent with the true values. However, the true value of $\hat{\psi}_2$ of P_2 is not in the interval $[0, 2\pi]$, and the estimated value will differ from the true value by an integer multiple of 2π, which is the "phase wrapping" phenomenon. However, since the estimations of $\hat{\psi}_1$ and $\hat{\psi}_2$ are not used in the estimation of the rotational radius and tilt angle, the effect of the phase error on the parameters estimation can be ignored. After the use of interference processing in the time-frequency domain and filtering, the OMP algorithm only needs to reconstruct four parameters, such as amplitude and initial phase of sinusoidal components with frequencies of $f_c + f_a$ and $f_c - f_a$, respectively. If the interference processing in the time-frequency domain and filtering are not carried out, the OMP algorithm needs to reconstruct four additional parameters, such as the amplitude and initial phase of the sinusoidal components with frequencies of f_c and f_c, respectively, which greatly increases the computational burden. Moreover, due to too many parameters to be searched, it is difficult for OMP algorithm to fully converge, which seriously affects the accuracy of micro-motion features extraction. Take scatterer P_1 as an example to analyze the advantages of interference processing in time-frequency domain and filtering in saving computing resources and improving estimation accuracy.

Without the interference processing in the time-frequency domain and filtering, the eight parameters reconstructed by the OMP algorithm and the estimated real rotational radius and tilt angle are shown in Table 3. In this paper, the running time is used as the evaluation criterion of computing resources. The comparison of normalized estimation error and running time of the two methods is shown in Table 4. It can be found that the use of time-frequency domain interference processing and filtering can save a lot of computation and improve the estimation accuracy of gyration radius and tilt angle by 3.14% and 5.65%, respectively.

Table 3. The decomposition results of the OMP algorithm without the interference processing in time-frequency domain and filtering.

Parameter	True Value	Estimated Value
$\hat{C}_1$	68.4 Hz	65 Hz
$\hat{C}_2$	9.8 Hz	8.0 Hz
$\hat{C}_3$	2216.4 Hz	2220 Hz
$\hat{C}_4$	16.4 Hz	14 Hz
$\hat{\psi}_1$	$\pi/3$ rad	0.3π rad
$\hat{\psi}_2$	$\pi/9$ rad	0.1π rad
$\hat{\psi}_3$	1.2014 rad	0.4π rad
$\hat{\psi}_4$	1.1071 rad	0.35π rad
$\hat{\theta}_e$	$\pi/6$ rad	0.4863 rad
$\hat{r}_a$	0.5 m	0.4707 m

Table 4. Comparison of normalized estimation error and running time of the two methods.

Method	Interference and Filtering		No Interference and Filtering	
Normalized estimation error	Rotational radius	Tilt angle	Rotational radius	Tilt angle
	2.73%	1.47%	5.87%	7.12%
Run time	29.52 s		1497.77 s	

4.2. Robustness Analysis

In order to verify the robustness of the proposed method, the influence of noise on the micro-motion parameters estimation is simulated and analyzed in this section. The noise added in this paper is additive white Gaussian noise (AWGN).

Firstly, the influence of noise on the accuracy of rotational frequency estimation is analyzed. Since the correlation of noise is very weak and the autocorrelation function of noise is almost zero, the estimation of rotational frequency by autocorrelation processing has better anti-noise performance. This simulation investigates the variation of the estimation error of rotational frequency with the SNR. When the SNR is −15 dB, the autocorrelation function of the micro-Doppler signal $f_d(t)$ is shown in Figure 8a. It can be seen that this function is greatly affected by noise and can not obtain an obvious peak value. When the SNR is −10 dB, the correlation function is shown in Figure 8b. The first obvious peak appears when the time is 0.1665 s. The rotational frequency can be estimated as 6.006 Hz. When the SNR is −5 dB, the correlation function is shown in Figure 8c. The first obvious peak occurs at t = 0.1667 s. The estimated value of rotational frequency is 5.9988 Hz. When the SNR changes from −15 dB to 5 dB, the variation of rotational frequency normalized error with the SNR is shown in Figure 9. It can be found that the rotational frequency estimation error decreases with the improvement of SNR.

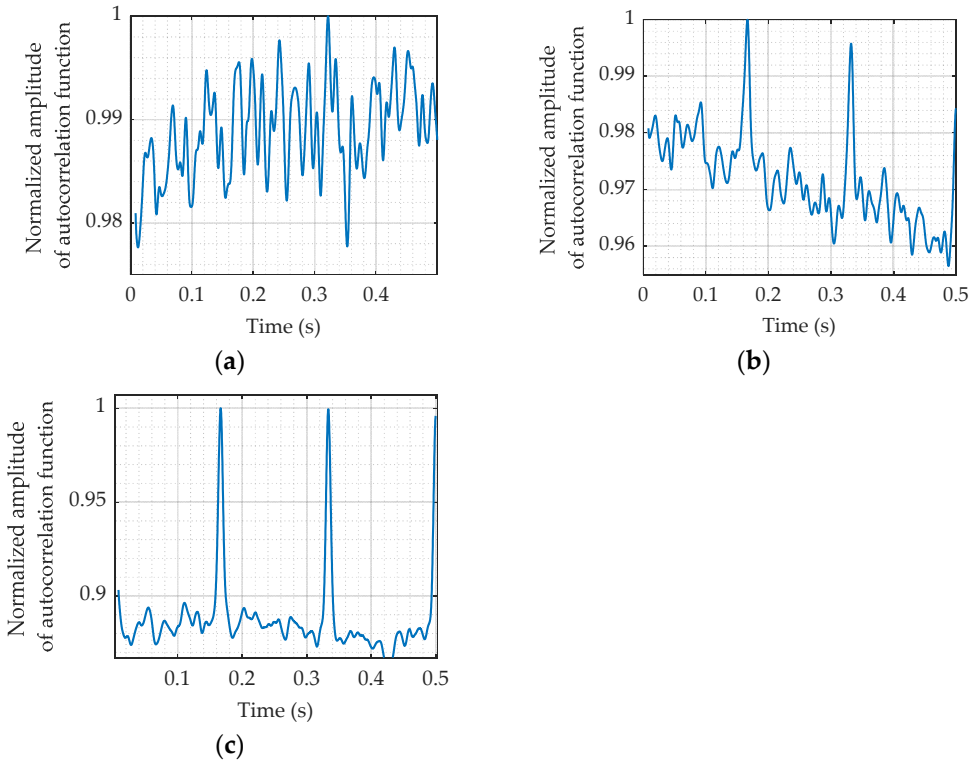

Figure 8. The autocorrelation function in different noise environments. The autocorrelation function when SNR is −15 dB (**a**); The autocorrelation function when the SNR is −10 dB (**b**); The autocorrelation function when SNR is −5 dB (**c**).

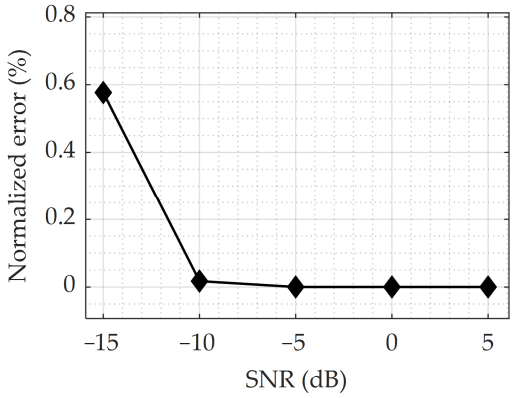

Figure 9. The variation of rotational frequency estimation error with the SNR.

In order to reduce the number of parameters to be reconstructed and save computing resources, the OMP algorithm is utilized on the basis of the estimated rotational frequency. Therefore, the estimation accuracy of rotational frequency will affect the reconstruction accuracy of the curves. The estimation accuracy of the rotational radius and tilt angle is shown in Figure 10 when the normalized estimation error of the rotational frequency changes from −8% to 8%. In general, the lower the rotational frequency estimation error is, the lower the impact on the other two parameters' estimation accuracy. When the rotational frequency estimation error is zero, the normalized error of the rotational radius and the tilt angle is the smallest. In particular, when the estimation error of the rotational frequency is −8%, the estimation error of the tilt angle is significantly higher than the estimation error of the rotational radius for the following two reasons: firstly, the estimation of the rotational radius is based on the estimation of the tilt angle, and Formulas (20) and (21) are nonlinear. The estimation error of the tilt angle may make the estimation error of the rotational radius larger, but it may also offset its estimation error in turn; secondly, the reconstructed result of the OMP algorithm is closely related to the initial search range and steps. Different initial values will make the OMP algorithm converge on different values of $\hat{C}_1$, $\hat{C}_2$, $\hat{\psi}_1$, and $\hat{\psi}_2$, thus causing the above phenomenon.

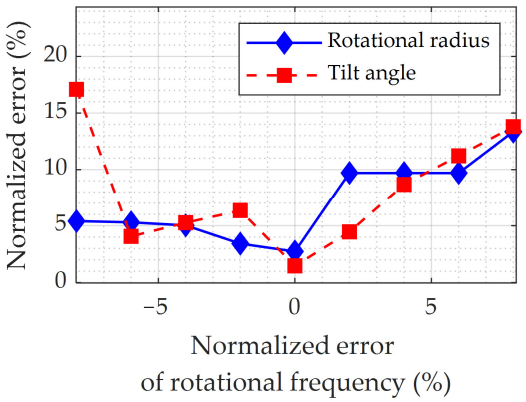

Figure 10. The variation of the real rotational radius and tilt angle estimation errors with the rotational frequency estimation error.

When the SNR is −5 dB, the results after interference processing in the time-frequency domain are shown in Figure 11a. The "burrs" on the curves after interference processing increases with the deterioration of the SNR. The results after smoothing are shown in Figure 11b. The final micro-Doppler curves after filtering are shown in Figure 11c. Due to the influence of noise, the micro-Doppler curves after interference processing in the time-frequency domain and filtering have some differences from the theoretical curves, which will have a greater impact on the reconstruction performance of the OMP algorithm.

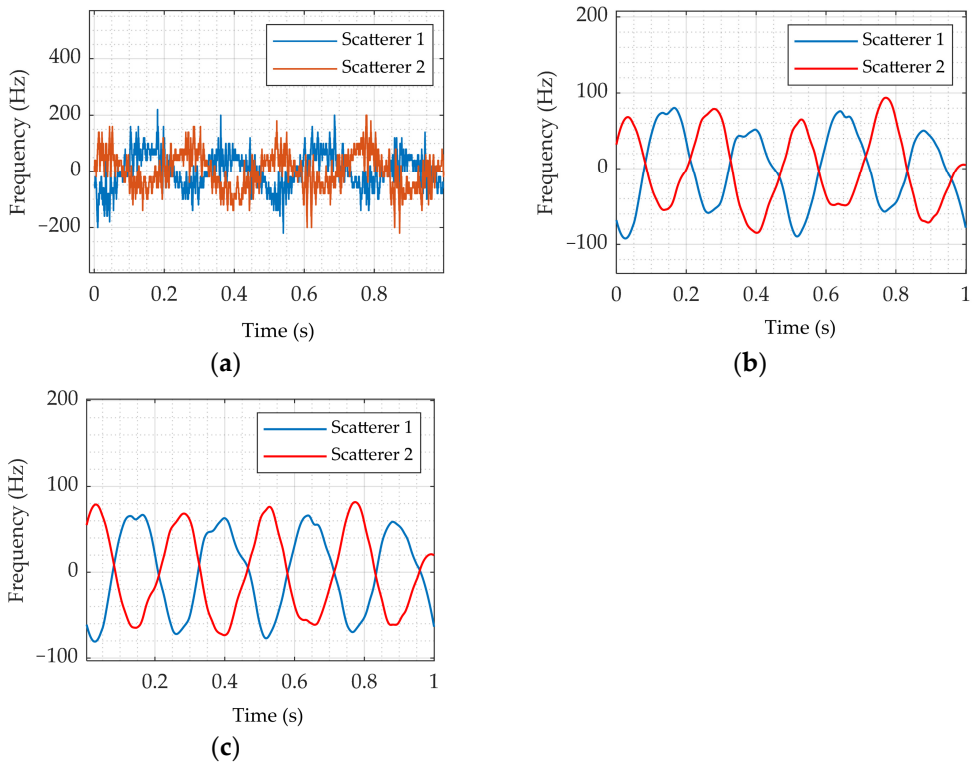

Figure 11. The micro-Doppler effect of the proposed method when the SNR is −5 dB. The results after the interference processing in time-frequency domain (**a**); The results after curves' smoothing (b); The micro-Doppler curves after filtering (**c**).

The OMP algorithm is utilized for the final curves, and the reconstructed curves parameters $(C_1, C_2, \psi_1, \psi_2)$ and the estimated values of real rotational radius and tilt angle are shown in Table 5. When the SNR is −5 dB, the average normalized errors of the real rotational radius and tilt angle are 4.78% and 9%, respectively. Therefore, the rotational frequency, real rotational radius, and tilt angle of the spinning target can still be estimated stably through the proposed method. When the noise environment deteriorates continuously from −5 dB, the discontinuous spots in the time-frequency diagram will increase. The skeletons do not meet the condition of smoothness. Therefore, curve separation can not be achieved, and the subsequent parameters estimation cannot be carried out.

Table 5. The decomposition results of the OMP algorithm and parameter estimation results when the SNR is −5 dB.

Parameter	Scatterer 1		Scatterer 2	
	True Value	Estimated Value	True Value	Estimated Value
$\hat{C}_1$	68.4 Hz	63.6 Hz	68.4 Hz	66.4 Hz
$\hat{C}_2$	9.8 Hz	11.2 Hz	9.8 Hz	8.0 Hz
$\hat{\theta}_e$	$\frac{\pi}{6}$ rad	0.5769 rad	$\frac{\pi}{6}$ rad	0.4814 rad
$\hat{r}_a$	0.5 m	0.4720 m	0.5 m	0.4802 m
$\hat{\psi}_1$	$\frac{\pi}{3}$ rad	0.35π rad	$\frac{4\pi}{3}$ rad	1.325π rad
$\hat{\psi}_2$	$\frac{\pi}{9}$ rad	0.125π rad	$-\frac{8\pi}{9}$ rad	1π rad

The SNR uniformly changes from −5 dB to 20 dB, and the experiment is repeated 100 times in each noise environment. The variation of the normalized estimation errors of the real rotational radius and tilt angle with the SNR is shown in Figure 12. It can be found that the normalized estimation errors of the micro-motion parameters decrease with the improvement of the SNR.

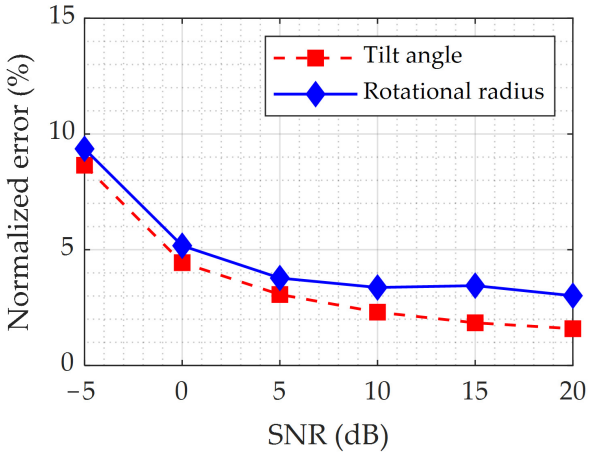

Figure 12. The variation of the real rotational radius and tilt angle estimation errors with the SNR.

4.3. Comparison with Other Methods

In order to highlight the uniqueness and superiority of the proposed method, the micro-Doppler parameter extraction methods of traditional monostatic radar and vortex-electromagnetic-wave-based radar are used to compare with the proposed method.

4.3.1. Comparison with the Monostatic Radar

The micro-Doppler effect of the spinning target is observed under different radar perspectives in this section. Monostatic radar can only obtain the radial micro-Doppler features. When the same target is observed, the micro-Doppler features under different radar perspectives are different, which will bring great trouble to the target classification and recognition. However, the proposed method can take advantage of the diversity of observation angles of the rotating antenna to obtain the real micro-motion parameters. As can be seen from Table 6, the amplitude of the micro-Doppler curves obtained by the monostatic radar is different when the tilt angle changes, which is the result of the mutual coupling of various micro-motion parameters. However, under the radar configuration proposed in this paper, the real rotational radius and tilt angle can still be estimated accurately. After obtaining more real information about the targets with micro-motions, the classification and recognition ability is expected to be effectively improved. The above comparison shows the superiority of the micro-motion parameter estimation method in this paper.

Table 6. The comparison of parameters extraction ability between the monostatic radar and the proposed method.

Parameter	**Tilt Angle (θ_e)**				
	$\frac{\pi}{3}$ **rad**	$\frac{\pi}{4}$ **rad**	$\frac{\pi}{5}$ **rad**	$\frac{\pi}{6}$ **rad**	$\frac{\pi}{10}$ **rad**
$\hat{\theta}_e$	1.0244 rad	0.7807 rad	0.6359 rad	0.5159 rad	0.3005 rad
$\hat{r}_a$	0.5225 m	0.5089 m	0.5096 m	0.5136 m	0.4870 m
$\hat{r}_{aLOS}$	0.4357 m	0.3552 m	0.2955 m	0.2438 m	0.1543 m

4.3.2. Comparison with the Vortex-Electromagnetic-Wave-Based Radar

By compensating the linear Doppler shift from the total Doppler shift, the linear Doppler and angular Doppler can be separated to estimate the rotational frequency, rotational radius, and tilt angle. Assuming that the OAM mode number l = 30, the PRF is 3000 Hz, and the other parameters are the same as those in Table 1. The conventional linear Doppler curve obtained by STFT is shown in Figure 13a, and the corresponding curve separation result is shown in Figure 13b. The total Doppler curve of the linear Doppler and angular Doppler mixture is shown in Figure 13c, and the corresponding curve

separation result is shown in Figure 13d. The angular Doppler curve can be obtained by subtracting the curve in Figure 13b from the curve in Figure 13d. The angular Doppler curve at this time has "burrs", as shown in Figure 13e. The angular Doppler curve after smoothing is shown in Figure 13f. By applying the EHT to the angular Doppler curve in Figure 13f, the rotational radius and tilt angle can be estimated. The estimated values of the rotational radius and tilt angle are 0.4760 m and 0.5320 rad, respectively, and the normalized estimation errors are 4.8% and 1.64%, respectively. The normalized estimation errors of the OAM-based method and the proposed method in this paper are both less than 5%. The number of antenna array elements (N) of the UCA should meet the condition of $-\frac{N}{2} < l < \frac{N}{2}$. Therefore, the number of array elements should be at least 61. However, on the one hand, the required cost is very high, and the radar system is very complex when N = 61. On the other hand, it is very difficult to reach the condition of l = 30 with the existing technology, and the purity of OAM mode cannot be guaranteed. In general, compared with the micro-Doppler parameter estimation method of vortex-electromagnetic-wave-based radar, the proposed method has greater advantages in feasibility at the present stage.

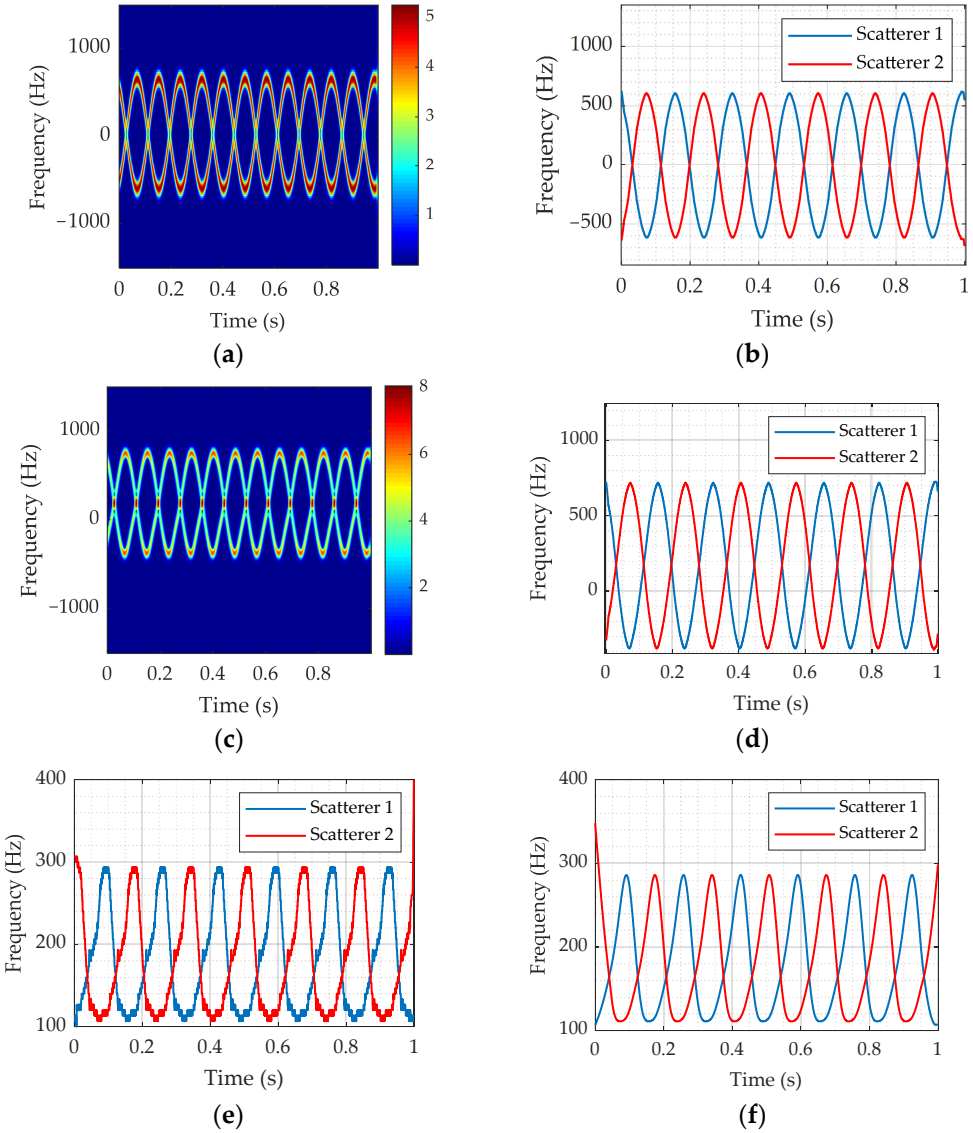

Figure 13. The micro-Doppler effect of the vortex-electromagnetic-wave-based radar. The STFT image of the linear micro-Doppler curve (**a**) and its curve separation result (**b**); The STFT image of the total micro-Doppler curve when l = 30 (**c**) and its curve separation result (**d**); The angular Doppler curve before smoothing (**e**) and after smoothing (**f**).

5. Conclusions

A new radar configuration based on the rotating interference antenna is proposed in this paper, which makes use of the various observation angles to estimate the real micro-Doppler parameters of the spinning targets. The simulation results show that the normalized estimation errors of the real rotational radius and tilt angle are less than 5% in the ideal environment. When the SNR is as low as -5 dB, the real micro-motion parameters of the spinning target can still be estimated stably by the proposed method. The proposed method provides a new idea to estimate the real micro-Doppler parameters, which is expected to improve the classification and recognition accuracy of the space target.

In addition, it can be seen from Equation (15) that the proposed method is limited by the detection range, which is the same problem as vortex-electromagnetic-wave-based radar. Recently, small rotor drones have been developing rapidly, which have the characteristic of low altitude. The proposed method is expected to obtain the real micro-motion parameters of the small rotor drones so as to carry out accurate classification and recognition. In the next step, the scattering point model and integral model of the rotor blade echo based on the rotating antenna will be established. The blade length, number of rotors, and tilt angle of the rotor targets will be extracted, and the classification and recognition performance will be analyzed.

Author Contributions: Conceptualization and methodology, Z.W.; software, Z.W. and H.Y.; resources, Y.L. and Y.C.; writing—review and editing, Z.W., Y.L., Y.C., H.Y. and Q.Z. All authors have read and agreed to the published version of the manuscript.

Funding: This research was funded by the postgraduate innovation practice foundation of Air Force Engineering University under Grant CXJ2021073 and the National Nature Science Foundation of China under Grant 61971434 and 62131020.

Data Availability Statement: Not applicable.

Acknowledgments: The authors would like to thank all reviewers and editors for their comments on this paper.

Conflicts of Interest: The authors declare no conflict of interest.

References

1. Chen, V.C.; Li, F.; Ho, S.S.; Wechsler, H. Micro-Doppler effect in radar: Phenomenon, model, and simulation study. *IEEE Trans. Aerosp. Electr. Syst.* **2006**, *42*, 2–21. [CrossRef]
2. Zhang, Q.; Hu, J.; Luo, Y.; Chen, Y. Research Progresses in Radar Feature Extraction, Imaging, and Recognition of Target with Micro-motions. *Radars. J.* **2018**, *7*, 531–547.
3. Persico, A.R.; Clemente, C.; Gaglione, D.; Ilioudis, C.V.; Cao, J.; Pallotta, L.; De Maio, A.; Proudler, I.K.; Soraghan, J.J. On Model, Algorithms, and Experiment for Micro-Doppler-Based Recognition of Ballistic Targets. *IEEE Trans. Aerosp. Electron. Syst.* **2017**, *53*, 1088–1108. [CrossRef]
4. Choi, O.; Park, S.H.; Kim, M.; Kang, K.B.; Kim, K.T. Efficient Discrimination of Ballistic Targets with Micromotions. *IEEE Trans. Aerosp. Electron. Syst.* **2020**, *56*, 1243–1261. [CrossRef]
5. Yang, D.; Wang, X.; Li, J.; Peng, Z. Micro-Doppler Curves Extraction of Space Target Based on Modified Synchro-Reassigning Transform and Ridge Segment Linking. *Remote Sens.* **2022**, *14*, 3691. [CrossRef]
6. Oh, B.S.; Lin, Z. Extraction of Global and Local Micro-Doppler Signature Features from FMCW Radar Returns for UAV Detection. *IEEE Trans. Aerosp. Electron. Syst.* **2020**, *57*, 1351–1360. [CrossRef]
7. Chen, X.; Zhang, H.; Song, J.; Guan, J.; Li, J.; He, Z. Micro-Motion Classification of Flying Bird and Rotor Drones via Data Augmentation and Modified Multi-Scale CNN. *Remote Sens.* **2022**, *14*, 1107. [CrossRef]
8. Hou, H.; Yang, Z.; Pang, C. Rotor UAV's Micro-Doppler Signal Detection and Parameter Estimation Based on FRFT-FSST. *Sensors* **2021**, *21*, 7314. [CrossRef]
9. Kang, K.B.; Choi, J.H.; Cho, B.L. Analysis of Micro-Doppler Signatures of Small UAVs Based on Doppler Spectrum. *IEEE Trans. Aerosp. Electron. Syst.* **2021**, *57*, 3252–3267. [CrossRef]
10. Björklund, S.; Petersson, H.; Hendeby, G. Features for micro-Doppler based activity classification. *IET Radar Sonar Navig.* **2015**, *9*, 1181–1187. [CrossRef]
11. Chen, Z.; Li, G.; Fioranelli, F.; Griffiths, H. Personnel Recognition and Gait Classification Based on Multistatic Micro-Doppler Signatures Using Deep Convolutional Neural Networks. *IEEE Geosci. Remote Sens. Lett.* **2018**, *15*, 669–673. [CrossRef]

12. Bai, X.; Hui, Y.; Wang, L.; Zhou, F. Radar-based human gait recognition using dual-channel deep convolutional neural network. *IEEE Trans. Geosci. Remote Sens.* **2019**, *57*, 9767–9778. [CrossRef]
13. Li, G.; Zhang, R.; Ritchie, M.; Griffiths, H. Sparsity-based dynamic hand gesture recognition using micro-Doppler signatures. In Proceedings of the 2017 IEEE Radar Conference (RadarConf), Seattle, DC, USA, 8–12 May 2017; pp. 928–931.
14. Zhang, Q.; Yeo, T.S.; Tan, H.S.; Luo, Y. Imaging of a Moving Target with Rotating Parts Based on the Hough Transform. *IEEE Trans. Geosci. Remote Sens.* **2008**, *46*, 291–299. [CrossRef]
15. Liu, K.; Cheng, Y.Q.; Li, X.; Jiang, Y.W. Passive OAM-Based Radar Imaging with Single-In-Multiple-Out Mode. *IEEE Micro. Wireless Compon. Lett.* **2018**, *28*, 840–842. [CrossRef]
16. Chen, R.; Zhou, H.; Moretti, M.; Wang, X.; Li, J. Orbital Angular Momentum Waves: Generation, Detection, and Emerging Applications. *IEEE Commun. Surv. Tutor.* **2020**, *22*, 840–868. [CrossRef]
17. Liang, J.; Zhang, Q.; Luo, Y.; Yuan, H.; Chen, Y. Three-Dimensional Imaging with Bistatic Vortex Electromagnetic Wave Radar. *Remote Sens.* **2022**, *14*, 2972. [CrossRef]
18. Zhou, Z.L.; Cheng, Y.Q.; Liu, K.; Wang, H.Q.; Qin, Y.L. Rotational Doppler Resolution of Spinning Target Detection Based on OAM Beams. *IEEE Sens. J.* **2019**, *3*, 1–4. [CrossRef]
19. Wang, Y.; Liu, K.; Wang, J.Q.; Wang, H.Q. Rotational Doppler detection of a cone-shaped target under the illumination of a vortex electromagnetic wave. *Radars. J.* **2021**, *10*, 740–748.
20. Luo, Y.; Chen, Y.J.; Zhu, Y.Z.; Li, W.Y.; Zhang, Q. Doppler effect and micro-Doppler effect of vortex-electromagnetic-wave-based radar. *IET Radar Sonar Navig.* **2019**, *14*, 2–9. [CrossRef]
21. Wang, Y.; Liu, K.; Liu, H.Y.; Wang, J.Q.; Cheng, Y.Q. Detection of Rotational Object in Arbitrary Position Using Vortex Electromagnetic Waves. *IEEE Sens. J.* **2021**, *21*, 4989–4994. [CrossRef]
22. Yuan, H.; Luo, Y.; Chen, Y.; Liang, J.; Liu, Y. Micro-motion parameter extraction of rotating target based on vortex electromagnetic wave radar. *IET Radar Sonar Navig.* **2021**, *15*, 1594–1606. [CrossRef]
23. Liu, K.; Liu, H.Y.; Qin, Y.L.; Cheng, Y.Q.; Wang, S.N.; Li, X.; Wang, H.Q. Generation of OAM Beams Using Phased Array in the Microwave Band. *IEEE Trans. Antennas Propag.* **2016**, *64*, 3850–3857. [CrossRef]
24. Liu, K.; Cheng, Y.Q.; Li, X.; Gao, Y. Microwave-Sensing Technology Using Orbital Angular Momentum: Overview of Its Advantages. *IEEE Veh. Technol. Mag.* **2019**, *14*, 112–118. [CrossRef]
25. Luo, Y.; Zhang, Q.; Yuan, N. Three-dimensional precession feature extraction of space targets. *IEEE Trans. Aerosp. Electron. Syst.* **2014**, *50*, 1313–1329. [CrossRef]
26. Luo, Y.; Zhang, Q.; Qiu, C.; Li, S.; Yeo, T.S. Micro-Doppler feature extraction for wideband imaging radar based on complex image orthogonal matching pursuit decomposition. *IET Radar Sonar Navig.* **2013**, *7*, 914–924. [CrossRef]